An Overmodulation Algorithm With Neutral-Point Voltage Balancing for Three-Level Converters in High-Speed Aerospace Drives

Feng Guo, *Student Member, IEEE,* Tao Yang, *Senior Member, IEEE,* Ahmed M. Diab, *Student Member, IEEE,* Seang Shen Yeoh, Chen Li, *Student Member, IEEE,* Serhiy Bozhko, *Senior Member, IEEE,* and Patrick Wheeler, *Fellow, IEEE*

***Abstract*—In this paper, a virtual space vector (VSV)-based overmodulation algorithm is presented for three-level neutral-point-clamped (3L-NPC) converters in high-speed aerospace motor drives. With the proposed inscribed polygonal-boundary compression technique, the output voltage capability is enhanced under a lower crossover angle and compression coefficient. As a result, it brings an opportunity for the operation of the studied aircraft electric starter/generator (ESG) systems easily extending from the linear modulation range into the overmodulation region. Furthermore, an active capacitor voltage balancing control method is investigated to recover neutral-point (NP) potential imbalance in the case of high modulation index and low power factor operating conditions. To simplify the digital implementation of the algorithm, a fast calculation approach is adopted in this work. The modulation performance of the proposed strategy is verified by both simulation and experimental results with a 45 kW, 32 krpm ESG prototype system.**

***Index Terms*—High-speed motor drives, more-electric-aircraft (MEA), neutral-point voltage, overmodulation, three-level.**

I. Introduction

THE concept of more-electric-aircraft (MEA) is attracting more and more attentions in the aerospace industry due to higher fuel efficiency, better environmental impact, suppressed audible noise and lower maintenance cost [1]-[3]. This cutting-edge technology aims at replacing pneumatic, hydraulic and mechanical power-driven systems by electrical counterparts in future aircraft [4]-[6]. An essential development for the MEA is the electric starter/generator (ESG) system. It can deal with several disadvantages that are common for state of the art starter/generator (S/G) systems [7]. Nowadays, the active rectification technology [8] opens opportunities for the integrated aircraft ESG systems which employ new machine types that are free from existing limitations and allow for the novel design of high-performance S/G systems in the MEA. The key component of the ESG system is a high-speed machine and a bidirectional converter, as shown in Fig.1. A permanent magnet synchronous machine (PMSM) is chosen since high torque-to-current ratio, high power density and high robustness can be achieved. Despite the fact that the efficiency of the machine can sometimes be improved by increasing pole number, the low carrier-pulse ratio issue becomes harsh, particularly for the converter-fed high-speed motor drives [9]. For this reason, a 6-pole 36-slot surface-mounted machine is chosen as the optimal candidate that also has the lowest eddy-current losses [8]. Compared with a typical two-level converter, the three-level neutral-point-clamped (3L-NPC) topology, as shown in Fig.2, is selected due to the utilization of lower blocking voltage switches, better output harmonic performance, and reduced EMI emissions.

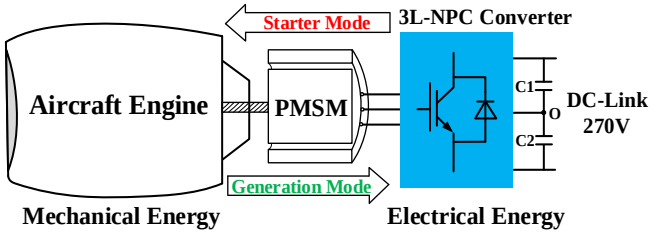

Fig. 1. ESG system of the more-electric-aircraft.

In the ESG system, the PMSM is mechanically coupled to an engine shaft via a gearbox and electrically connected with a 3L-NPC converter which interfaces the S/G system to the onboard electric power system. In the startup process, the converter serves as an inverter that drives the PMSM to crank and accelerate engine shaft. Once the engine is up to a self-sustained speed, the engine ignition activates. After that, the ESG system goes into standby mode. When the PMSM shaft speed approaches 20 krpm, the generation mode starts. In this mode, the engine drives the machine to generate electrical power, and the converter works as a rectifier to convert the variable frequency AC into DC that supplies onboard loads.

Due to the high-speed operation of the machine, the converter uses deep flux-weakening control to ensure that the back electromotive force (EMF) is within converter limits. However, not only large flux-weakening currents cause more machine copper losses but also the output electromagnetic torque capability in the constant power region is weakened as the speed of PMSM increases, and is constrained by stator voltage. In addition, the 3L-NPC topology has an inherent NP potential deviation because of the split DC-link capacitor bank, which results in extra over-stress across switching devices and output distortion, particularly for the ESG system operating in stringent conditions, i.e., high modulation index and low power

This work was supported by the Clean Sky 2 Joint Undertaking under Grant 807081. (*Corresponding author: Tao Yang*.) The author Feng Guo would like to thank China Scholarship Council (CSC) for sponsoring part of his Ph.D studentship.

F. Guo, T. Yang, S. S. Yeoh, C. Li, S. Bozhko and P. Wheeler are with the Power Electronics, Machines and Control Group, the Department of Electrical and Electronic Engineering, The University of Nottingham, Nottingham, NG7 2RD, U.K. (email: feng.guo@nottingham.ac.uk; tao.yang@nottingham.ac.uk; seang.yeoh@nottingham.ac.uk; chen.li@nottingham.ac.uk; serhiy.bozhko @nottingham.ac.uk; pat.wheeler@nottingham.ac.uk)

Ahmed M. Diab is with the Key Laboratory of More Electric Aircraft Technology of Zhejiang Province, University of Nottingham Ningbo China, Ningbo 315100, China (e-mail: ahmed.diab@nottingham.edu.cn)

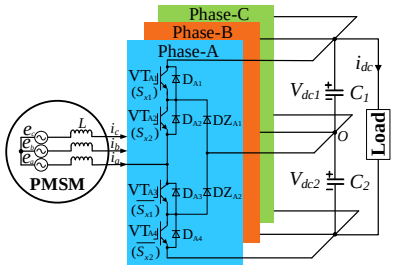

Fig. 2. The structure of 3L-NPC power converter-fed PMSM drives.

factor. Consequently, these significant challenges are required to be settled for high-performance three-level converter-fed high-speed aerospace motor drives in MEA applications.

In recent years, numerous advanced pulse-width-modulation (PWM) strategies have been studied to tackle the unbalanced capacitor voltage problem in 3L-NPC converters [10]-[12]. Besides, the model predictive control (MPC)-based NP voltage balancing methods [13], [14] are incorporated in the space-vector-PWM (SVM) modulator to obtain exceptional dynamic performance of systems. Compared with the aforesaid approaches, the nearest-three virtual space vector (NTV^2) modulation concept presented in [15] is more attractive as it achieves inherent NP voltage balance for all loads. Although the advantage is at the expense of additional switching losses, more degrees of freedom by this technique can bring other merits, such as common-mode voltage (CMV) reduction [16].

To boost the DC-link voltage utilization, a number of overmodulation algorithms have been developed by researchers for two-level [17]-[20], flying capacitor [21], [22], cascaded [23], [24] and diode-clamped [25]-[32] multilevel inverters. The existing literature about the overmodulation strategy for the NPC topology is discussed in the following. In [25], the authors propose an overmodulation method by calculating three-phase modulation waves, which is beneficial for simple implementation in digital controllers. With the help of the neural-network, a classification SVM technique [26] in overmodulation region has been studied for 3L-NPC converters, which ensures a smooth linear transition and lower complexity. It is noted that the authors employ the nearest-three space vector (NTV) scheme and predefine a series of switching sequences to maintain two capacitor voltages. For the high-power applications with a low pulse-ratio, a synchronized SVM strategy [27] is proposed to operate induction motor drives in the overmodulation region. In order to avoid trigonometric computations, a duty cycle-based overmodulation strategy is presented in [28], together with a dedicated NP voltage balancing control method. In [29], a timing-correction based algorithm is investigated to gain the output voltage under overmodulation conditions. Also, the approach is implemented in a field-programmable-gate-array (FPGA)-based real-time control platform to attain the minimum computational resources. With respect to low power factor loads, however, the aforementioned methods pose a challenge for capacitor voltage balance, as well as elimination of low-frequency NP potential oscillation. To address these deficiencies, a hybrid SVM strategy is introduced in [30] to operate a 3L-NPC inverter in the overmodulation region. This approach abandons medium vectors to mitigate voltage fluctuation in the NP, but harmonics performance of phase current may suffer from non-nearest-three-vectors in a higher output voltage region. In [31], a carrier-based PWM (CBPWM) scheme for 3L-NPC inverter-fed induction motor drive systems with dynamic loads has been studied to extend the operating point into the overmodulation region. Besides, the technique is capable of keeping two capacitor voltage in a balanced state when NP potential deviation occurs. It is worth noting that calculating an appropriate zero-sequence voltage components is required. The work reported in [32] discusses a novel overmodulation scheme that achieves the balanced capacitor voltages and alleviated low-frequency NP voltage fluctuation over the entire range of modulation indices and power factor angles, even for n-level NPC topologies. While the performance is desirable by applying VSVs, maintaining capacitor voltage balanced is not discussed when NP voltage shifts. Additionally, the presented hexagonal compression limit may impair overmodulation capability to some extent.

In this paper, a new variant of the VSV-based PWM algorithm is proposed for the operation of aircraft ESG systems extending into the overmodulation region. Compared with the prior method [32], the presented trajectory of the reference voltage vector contributes to a better overmodulation capability for converter-fed high-speed aerospace motor drives. With the introduced NP potential balancing control strategy, two capacitor voltages are effectively kept at a balanced state if NP voltage drifts away. Notably, the technique is easily implemented with a fast calculation approach, which aims to reduce the computational complexity for the digital controller.

The rest of this paper is organized as follows. The principles of the ESG system are briefly introduced in Section II. The proposed capacitor voltage balancing control-based overmodulation algorithm is studied in Section III. Simulation and experimental results are presented in Section IV to evaluate the modulation performance. Finally, the main conclusions of this work are summarized in Section V.

II. Principles of ESG System

A. PMSM Model and Operating Constrains

The PMSM mathematical model equations in the *d-q* coordinates are expressed as follows:

$$T_{em} = \frac{3}{2} n_p \cdot [\varphi_f \cdot i_q + (L_d - L_q) \cdot i_d \cdot i_q] \tag{1}$$

$$V_d = R \cdot i_d + L_d \frac{di_d}{dt} - \omega_e \cdot L_q \cdot i_q \tag{2}$$

$$V_q = R \cdot i_q + L_q \frac{di_q}{dt} + \omega_e \cdot L_d \cdot i_d + \omega_e \cdot \varphi_f \tag{3}$$

where T_{em} represents the electromagnetic torque, n_p refers to the number of pole pairs, φ_f is the permanent magnet flux linkage, V_d, V_q and i_d, i_q indicate the direct and quadrature components of motor voltage and current, respectively, L_d and L_q are the *dq*-axis inductances, ω_e denotes electrical angular frequency and R is the stator winding resistance.

For the applied surface-mounted PMSM in the ESG system, L_d equals L_q. Hence, the electromagnetic torque of machine is only provided by permanent magnet torque, which is the

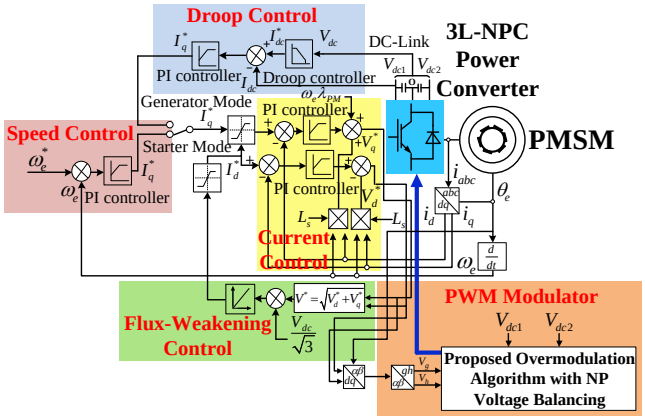

Fig. 3. Control blocks of the developed ESG system.

TABLE I
SWITCHING STATES AND OUTPUT VOLTAGES OF 3L-NPC CONVERTERS

Switching States	Gating Signals (S_{x1},S_{x2})	Output Voltages
[P]	(1, 1)	$V_{dc}/2$
[O]	(0, 1)	0
[N]	(0, 0)	$-V_{dc}/2$

first term in (1). Since the maximum machine stator voltage, indicated by V_{lim}, is determined by DC-link voltage and PWM strategy, the corresponding limitation can be written as:

$$(i_d + \frac{\varphi_f}{L_d})^2 + i_q^2 = (\frac{V_{lim}}{\omega_e L_q})^2 \tag{4}$$

Considering the capacity of designed machine/converter, the maximum current value, manifested by I_{max}, should fulfill:

$$i_d^2 + i_q^2 \le I_{max}^2 \tag{5}$$

The solution of (4) and (5) is an overlapped area of voltage and current limit circle, which therefore restrict the allowable operating points of the ESG system.

B. Control Design of ESG System

The whole system control block includes flux-weakening, machine speed, current loop and droop control, as illustrated in Fig.3. Speed control is activated in the startup process. DC-link current is manipulated by droop characteristics in the generation mode. The vector control technique is used for machine decoupling purpose, which allows controlling flux and torque independently. Therefore, machine torque represented as active power is controlled by q-axis current. As the maximum phase voltage is limited by a definite DC-link voltage supply of 270VDC, a large negative current needs to be injected into d-axis during the high-speed operation, which results in a lower power factor angle.

C. Three-Level NPC Converter, SVM Strategies and NP Voltage Imbalance Issue

As shown in Fig.2, each phase of the converter consists of four semiconductor devices (VT_{x1}~VT_{x4}) and two clamping diodes (DZ_{x1} and DZ_{x2}), where x∈{A, B, C}. Two equal capacitors (C_1 and C_2) are series-connected to form the DC-link. VT_{x1} is complimentarily switched with VT_{x3}. VT_{x2} and VT_{x4} follow the same manner. The switching state [P] means gating signal (S_{x1},S_{x2}) is (1,1), which represents output voltage of V_{dc}/2. The switching state [N] manifests gating signal

TABLE II
THE MAGNITUDE OF SPACE VECTORS

Space Vectors	Magnitude
Zero Vector	0
Small Vector	$V_{dc}/3$
Medium Vector	$\sqrt{3}V_{dc}/3$
Large Vector	$2V_{dc}/3$

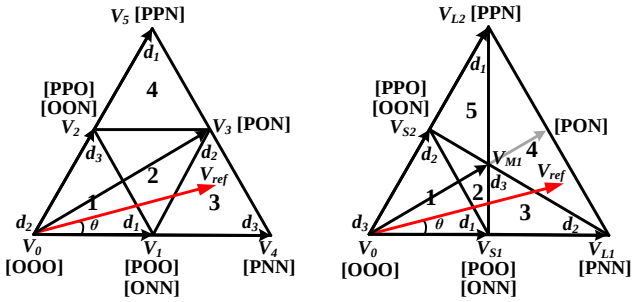

(a) (b)

Fig. 4. The space vector diagram of: (a) NTV scheme. (b) NTV^2 scheme.

(S_{x1},S_{x2}) is (0,0), which denotes output voltage of $-V_{dc}/2$, where V_{dc} refers to the full DC-link voltage. Otherwise, gating signal (S_{x1},S_{x2}) is chosen as (0,1), the output voltage is zero and switching state is expressed as [O]. The switching principle of the 3L-NPC converter is detailed in Table I.

With regard to the magnitude of space vectors listed in Table II, 27 switching states generated by the converter can be grouped into four categories: zero, small, medium and large vectors, wherein 12 are small ones while the number of large and medium ones are both 6, and the rest are zero vectors.

It is assumed that the reference voltage vector is located in the subsector 3 of Sector-I. The NTV scheme uses V_1, V_3 and V_4 to synthesize V_{ref}, as shown in Fig.4(a). According to the volts-second balance rule, (6) can be obtained:

$$\begin{cases} V_{ref} = V_1 \cdot d_1 + V_3 \cdot d_2 + V_4 \cdot d_3 \\ d_1 + d_2 + d_3 = 1 \end{cases} \tag{6}$$

where d_1, d_2 and d_3 indicate the duty cycle of V_1, V_3 and V_4, respectively.

And then, the solution of above equations can be yielded:

$$\begin{cases} d_1 = 2[1 - m \cdot \sin(\pi/3 + \theta)] \\ d_2 = 2m \cdot \sin(\pi/3 - \theta) \\ d_3 = 2m \cdot \sin(\pi/3 - \theta) - 1 \end{cases} \tag{7}$$

where θ represents reference voltage vector rotating angle, m refers to the modulation index defined by:

$$m = \frac{|V_{ref}|}{V_{dc}/\sqrt{3}} \tag{8}$$

Here, the four-state synthesis approach, i.e., reference voltage vector is composed of four switching states from the selected NTVs, is adopted to discuss the NP voltage imbalance issue. For example, if V_{ref} falls into subsector 3 of Sector-I, the time-averaged NP current is given by:

$$\overline{I_{NP}} = \sigma \cdot d_{onn} \cdot i_a + d_{pon} \cdot i_b + (1 - \sigma) \cdot d_{poo} \cdot (-i_a) \tag{9}$$

where σ∈$[0, 1]$ denotes a distribution factor of redundant small vector pairs.

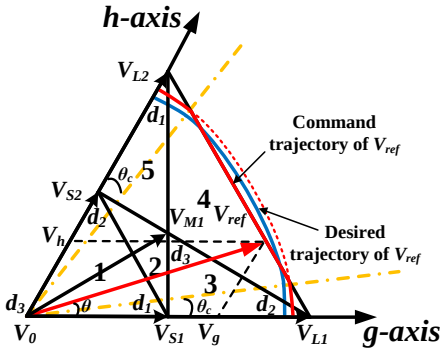

Fig. 5. VSV-based PWM scheme for operating OM-I in Sector-I.

Thus, the capacitor voltage deviation for each switching period can be calculated as:

$$\Delta V_{dc} = \frac{1}{C}\int_{t=0}^{t=T_s} \overline{I_{NP}} \cdot dt \tag{10}$$

where C and T_s represent the DC-link capacitance and a switching period, respectively.

By regulating σ in (9), NP currents produced by small vectors can be used to compensate for the accumulated NP potential rendered by medium vectors. However, it should be pointed out that the strength of capacitor voltage balancing becomes weak when the modulation index arises to unity and power factor angle towards $\pm 90°$ [12].

In contrast, the NTV^2 scheme employs a series of VSVs that is modified by basic space vectors with a specific proportion. The definition of zero and large vectors, denoted as V_0, V_{L1} and V_{L2}, are the same as the NTV scheme, whereas V_{S1}, V_{S2} and V_{M1} are virtual small and medium vectors defined by:

$$\begin{cases} V_{S1} = (V_{[\mathrm{POO}]} + V_{[\mathrm{ONN}]})/2 \\ V_{S2} = (V_{[\mathrm{PPO}]} + V_{[\mathrm{OON}]})/2 \\ V_{M1} = (V_{[\mathrm{ONN}]} + V_{[\mathrm{PON}]} + V_{[\mathrm{PPO}]})/3 \end{cases} \tag{11}$$

When V_{ref} falls into subsector 4 of Sector-I, as shown in Fig.4(b), the corresponding duty cycle is calculated as:

$$\begin{cases} d_1 = 3[1 - m \cdot \sin(\pi/3 + \theta)] \\ d_2 = \sqrt{3} m \cdot \cos\theta - 1 \\ d_3 = \sqrt{3} m \cdot \sin(\pi/6 + \theta) - 1 \end{cases} \tag{12}$$

As the polarity of NP currents associated with redundant small vector pairs are opposite and the sum of balanced three-phase currents is zero, VSVs have no impact on NP potential deviation. Therefore, the NTV^2 scheme achieves two balanced capacitor voltages for all load conditions.

III. Proposed VSV-Based Overmodulation Algorithm

In accordance with the modulation index defined by (8), the operating regions of a converter can be classified into three parts: linear modulation (LM), overmodulation mode-I (OM-I), and overmodulation mode-II (OM-II).

In the LM region, the reference voltage vector traces a circular trajectory inside the hexagon. Accordingly, modulation index ($0 \le m \le 1$) arises with increasing magnitude of output voltage until the trajectory is inscribed in the hexagon side.

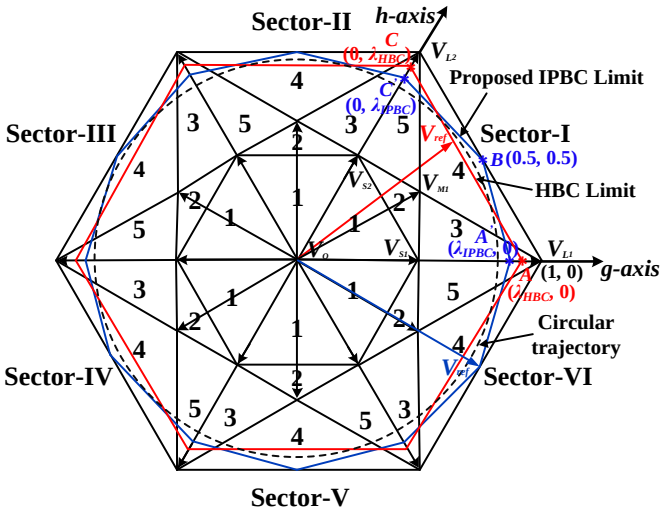

Fig. 6. Space vector diagram of polygonal-boundary limits for VSV-based PWM scheme.

TABLE III
Duty Cycle of VSVs for Subsector 1-5 of Sector-I

Subsector	d_1	d_2	d_3
1	$2g$	$2h$	$1-2(g+h)$
2	$2(1-g-2h)$	$2(1-h-2g)$	$3[2(g+h)-1]$
3	$2(1-2h-g)$	$2g+h-1$	$3h$
4	$2h+g-1$	$2g+h-1$	$3(1-g-h)$
5	$2(1-2g-h)$	$2h+g-1$	$3g$

Within linear range, the duty cycle for each space vector can be calculated by (6). The OM-I denotes the radius of desired reference voltage vector is between the inscribed circle and circumscribed circle of the hexagon, which indicates a higher achievable modulation index ($1 < m \le 1.05$). In this mode, the tip of modified reference voltage vector transits from a circular trajectory and moves along the hexagon side when it exceeds the boundary of hexagon. Thus, a crossover angle (θ_c) that keeps the trajectory inside half of the sextant needs to be controlled for obtaining adequate modulation depth, as shown in Fig.5. To further increase modulation index, the reference voltage vector is fixed at the vertex for a period of time, and then jumps to the straight line of the hexagon by a holding angle (θ_h). When θ_h equals 30°, the discrete six-step mode operates, which constrains m_{max} of OM-II at 1.1 [17].

Since the output variables of a converter steeply deteriorate in the OM-II [18], [20], the acoustic noise and torque ripple issues are much severe, which is not suitable for the applications of high-speed aerospace motor drives. As a result, the scope of this study primarily focuses on the operation of OM-I, which provides a chance to achieve higher DC-link voltage utilization, enhance output torque capability, and reduce large-required flux-weakening current for the aircraft ESG system. For the purpose of simplifying PWM calculation process, the proposed VSV-based overmodulation algorithm is carried out in a transformed reference frame. The detailed descriptions of each subsection are given in the following.

A. The Fast Calculation Approach

With (13), the traditional orthogonal plane can be shifted into a sextant one for simplifying the duty cycle expression using trigonometric functions.

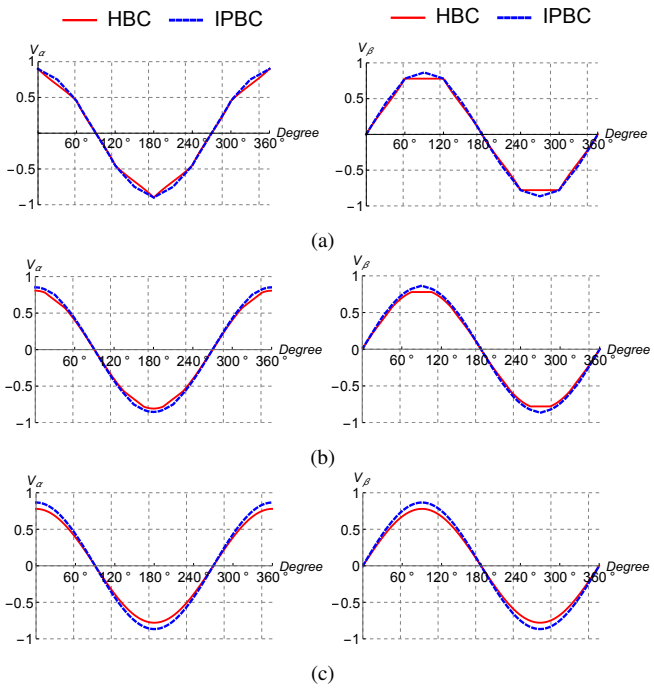

Fig. 7. V_α and V_β with: (a) $\theta_c = 0°$. (b) $\theta_c = 15°$. (c) $\theta_c = 30°$.

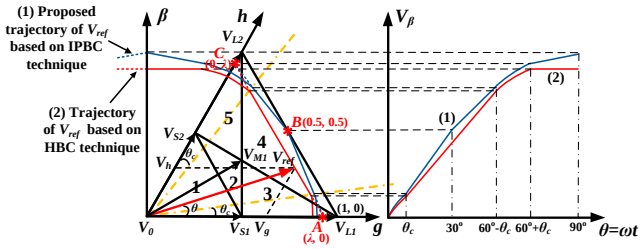

Fig. 8. The trajectory of modified V_{ref} and corresponding V_β waveforms.

$$\begin{bmatrix} V_g \\ V_h \end{bmatrix} = \begin{bmatrix} 1 & -1/\sqrt{3} \\ 0 & 2/\sqrt{3} \end{bmatrix} \begin{bmatrix} V_\alpha \\ V_\beta \end{bmatrix} \tag{13}$$

By projecting (6) into this frame, V_g and V_h are yielded as:

$$\begin{cases} V_g = X_g d_1 + Y_g d_2 + Z_g d_3 \\ V_h = X_h d_1 + Y_h d_2 + Z_h d_3 \end{cases} \tag{14}$$

where (V_g,V_h), (X_g,X_h), (Y_g,Y_h) and (Z_g,Z_h) are the coordinates of V_{ref} and three VSVs in the g-h plane, respectively.

In addition, it is notable that all VSVs and V_{ref} are normalized with respect to the magnitude of large vector $(2V_{dc}/3)$. Hence, (V_g,V_h) can be conveniently expressed as (g,h) in the following derivation. Overall, the duty cycle of each VSV in all subsectors of the first sector is detailed in Table III, where $d_1 \sim d_3$ are displayed in Fig.4(b).

B. The Inscribed Polygonal-Boundary Compression Technique

As mentioned above, before tracking circular trajectory in linear range again, the reference voltage vector command is programmed to coincide with the hexagon side for the purpose of a higher fundamental component in output voltage. As seen from Fig.5, with the geometric relationships of VSV-based SVM, the following equations are given:

$$\begin{cases} \dfrac{|V_{ref}|_{p.u}}{\sin 120°} = \dfrac{g}{\sin(60° - \theta)} = \dfrac{h}{\sin\theta} \\ \dfrac{1}{\sin(120° - \theta)} = \dfrac{|V_{ref}|_{p.u}}{\sin 60°} \end{cases} \tag{15}$$

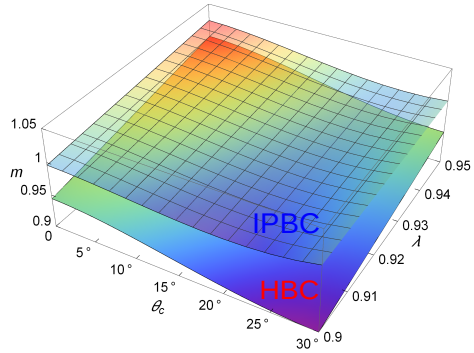

Fig. 9. The 3D plot of $m(\theta_c, \lambda)$ with the HBC and IPBC technique.

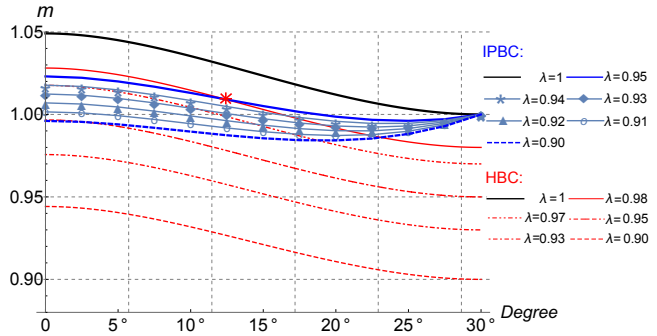

Fig. 10. The relationship between m and θ_c at different λ.

To approximate the red straight-line in Fig.5, the duty cycle of each VSV can be easily calculated by Table III and (15). As shown in the Appendix, however, the dwell time of virtual medium vector (d_3T_s) constantly equals zero at that time. It means that only large vectors are used, which therefore violates the three-level operation of the converter. This phenomenon not only lowers the efficiency of the ESG system but also incurs a steady-state capacitor voltage error if NP potential imbalance initially exists. To address the demerit, the hexagon side was scaled down by a compression coefficient λ [32]. Thus, it makes full use of virtual medium vector and takes its dwell time to $3(1-\lambda)$, as derived in the Appendix. Fig.6 shows the space vector diagram of polygonal-boundary limit, in which the red straight-line denotes the prior hexagonal-boundary compression (HBC) limit [32] that is formed by A(λ_{HBC},0) and C(0,λ_{HBC}) in the first sextant.

In order to fully utilize the margin of the hexagon, not only the tip of V_{ref} passes through A$'$(λ_{IPBC},0) and C$'$(0,λ_{IPBC}), but also the middle point of hexagon side is involved, as shown in Fig.6, which is an inscribed polygonal-boundary compression (IPBC) limit represented by a blue dodecagon and forms the basis of the proposed solution. For example, B(0.5,0.5) is a turning point for Sector-I. It is worth noting that both two boundaries gradually coincide with the hexagon side when the compression coefficient converges to 1, and output voltage eventually reaches the upper limit of OM-I.

For a given λ, the presented trajectory of normalized $|V_{ref}|$ in a quarter cycle is given by:

$$|V_{ref}|(\theta) = \begin{cases} \dfrac{\sigma}{\sin[\theta + \arcsin\sigma]} & 0 \le \theta < 30° \\ \dfrac{\sigma}{\sin[60° - \theta + \arcsin\sigma]} & 30° \le \theta < 60° \\ \dfrac{\sigma}{\sin[\theta - 60° + \arcsin\sigma]} & 60° \le \theta < 90° \end{cases} \tag{16}$$

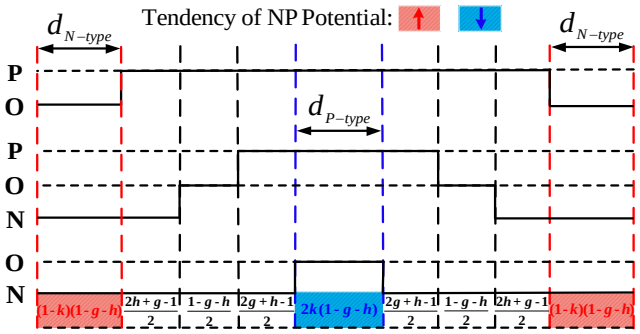

Fig. 11. The modified switching instant for NP voltage balancing control in subsector 4 of Sector-I.

where $\sigma=\dfrac{\sqrt{3}/4 \times \lambda}{\sqrt{\lambda^2 - 3/2\lambda + 3/4}}$ and $\theta=\omega t$ (ω is the angular fundamental frequency).

Given that the selected compression coefficient is 0.9, the $\alpha\beta$-axis components of the proposed technique and its counterpart under different θ_c are shown in Fig.7, in which red and blue waveforms refer to V_α and V_β generated by the HBC and IPBC scheme. As shown, the proposed approach makes these two components more sinusoidal. Hence, it would be expected to attain less distortion in output voltage and current.

The introduced track of V_{ref} with its output phase voltage in β-axis is shown in Fig.8. The amplitude of its fundamental component can be thus calculated by Fourier series expansion:

$$F(\theta) = \frac{\pi}{4} \int_{0^\circ}^{90^\circ} |V_{ref}|(\theta) \cdot \sin\theta \cdot d\theta \tag{17}$$

With (17), the desired modulation indices with different compression coefficients and crossover angles can be attained and described by Fig.9 and Fig.10. As shown, the DC-link voltage utilization of the IPBC scheme is higher than that of the HBC scheme under the same conditions. In other words, λ and θ_c of the proposed technique are allowed to be set at a smaller value to achieve the same overmodulation capability as the prior method. Besides, it can be seen that m_{max} of the proposed approach is the same as that of the counterpart.

C. NP Voltage Balancing Control

Although the applied VSVs can maintain NP voltage naturally balanced irrespective of modulation index and power factor angle, the voltage balance between two capacitors cannot be facilitated by itself if the initial NP potential imbalance exists under overmodulation conditions. Therefore, active capacitor voltage balancing control must be involved to handle the divergence. When extra electric charges are accumulated in the last control period, the capacitor voltage shifts. With (10), the required NP electric charge for the convergence of capacitor voltage within a sampling time can be expressed as:

$$0 = C \cdot \Delta V_{dc} + \Delta Q \tag{18}$$

where ΔQ is defined as the compensated charge.

To meet the above requirement, a straightforward solution is to manipulate the dwell time of space vectors that can provide NP current with appropriate polarity. Moreover, it is known that when the converter runs for rectifying, NP potential tends to arise up with more participation of N-type small vectors and vice versa. Hence, according to the operational mode of the ESG system and DC-bias in the NP, the dwell time of these

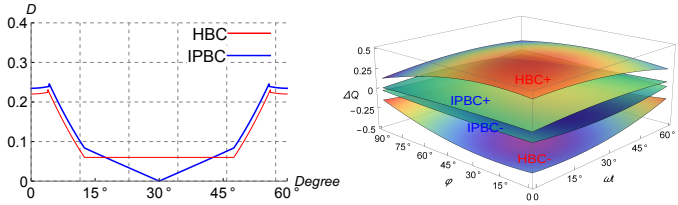

(a) (b)

Fig. 12. The comparison of NP voltage balancing capability: (a) Active duty cycle of VSVs. (b) ΔQ as a function of power factor ϕ and ωt.

vectors for composing VSVs can be regulated by an allocation coefficient k, as given by (19), where V_{dc1} and V_{dc2} indicate the upper and lower-side capacitor voltage, respectively.

$$k = \frac{V_{dc1}}{V_{dc1} + V_{dc2}} \in [0, 1] \tag{19}$$

When V_{ref} falls into subsector 4 of Sector-I, the modified switching intervals under overmodulation conditions are shown in Fig.11, in which (g,h) is the real-time coordinate of the blue line in Fig.6. To evaluate the ability of the introduced NP voltage balancing control method, the fundamental component of output voltage should be set at the same value. For example, the compression coefficient of HBC and IPBC limit are 0.98 and 0.95, respectively, and the crossover angle is set to be 12.5°. By doing so, the desired modulation indices are both at 1.01, and the reference voltage vector is synthesized in subsectors 3-5. Here, Sector-I is chosen as a representative example to investigate. The dwell time of active VSVs and the compensated charge ΔQ based on (10) and (18) are illustrated in Fig.12(a) and Fig.12(b), respectively, in which '+' and '−' represent the maximum and minimum value by corresponding approaches. As can be seen, although the compensation capability of the presented IPBC technique is a bit weak as compared to that of the prior method, it can still resolve the NP voltage imbalance issue for all loads.

Noteworthy, the output line-to-line voltage might be distorted by the modified duty cycles of small vectors to some extent. Nevertheless, it facilitates a trade-off between capacitor voltage balance and short-term output harmonic performance. In addition, the distortion caused by the onsite closed-loop control will be quickly dismissed when the NP potential is maintained at a balanced state again.

IV. Performance Analysis

In this section, the performance of the proposed overmodulation algorithm is validated by simulation and experimentation. The 3L-NPC converter-fed PMSM drive systems are simulated in the Simulink/PLECS environment. The ESG system initially runs in the startup process. The flux-weakening control is triggered at 0.5s. The power generating mode starts by connecting a 10 kW resistive load to the DC-link at 1s. The presented approach is activated at 1.1s. The experimental validation is tested on a 45 kW, 32 krpm laboratory-built ESG prototype system, as shown in Fig.13. A 150 kW prime mover that emulates aircraft engine shaft and an oil-cooled high-speed machine are located in an isolated room for the safety viewpoint. The controller platform uses a TMS320C6713 chip and an Actel FPGA-ProAsic3 A3P400 kit. The torque of the

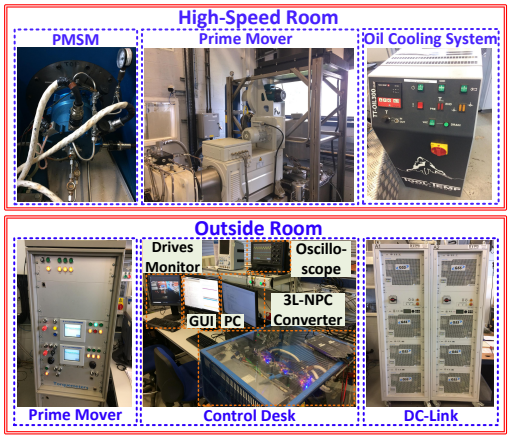

Fig. 13. ESG system test rig.

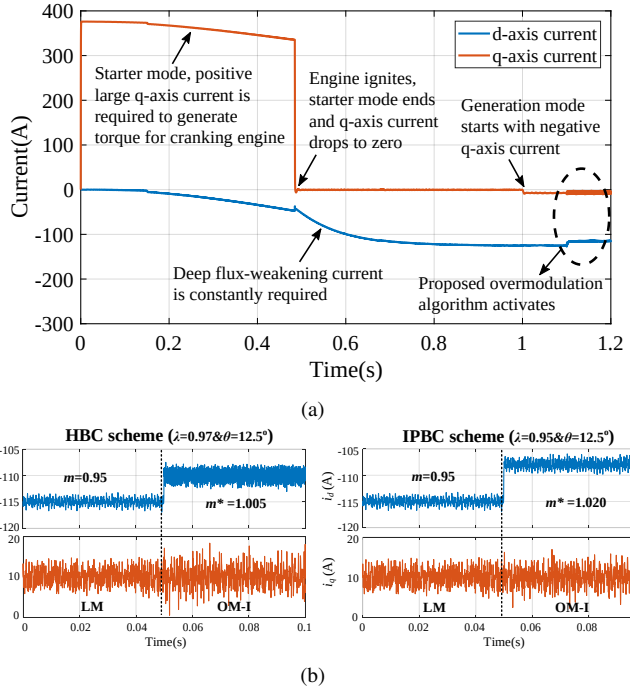

Fig. 14. (a) Simulated *dq*-axis current of the ESG system under the proposed technique. (b) Experimental results of the *dq*-axis currents.

PMSM is measured by ET1303 Torquemeter. *dq*-axis currents are displayed by the Graphic User Interface (GUI) software. AC-side parameters are monitored by PPA5530 power analyzer. Since the direction of phase current changes rapidly in light-load conditions, it weakens NP voltage balance in the OM-I. Thus, the experimental verifications mainly focus on the motor drives operating in the overmodulation region during the generation mode, particularly in a light-load condition, whereas the results in the starter mode are not presented as it accounts for a short time compared with the whole operation time. The system parameters are detailed in Table IV.

A. Improvement of DC-link Voltage Utilization

Without loss of generality, θ_c of the proposed strategy is set at 12.5° and λ is chosen as 0.95. The simulation results of *dq*-axis currents illustrated in Fig.14(a) describe the required torque and flux-weakening currents for the motor drives in entire speed range operation. As shown, i_d is significantly reduced after 1.1s. It indicates that the IPBC scheme offers a higher DC-link voltage utilization, thereby extending the

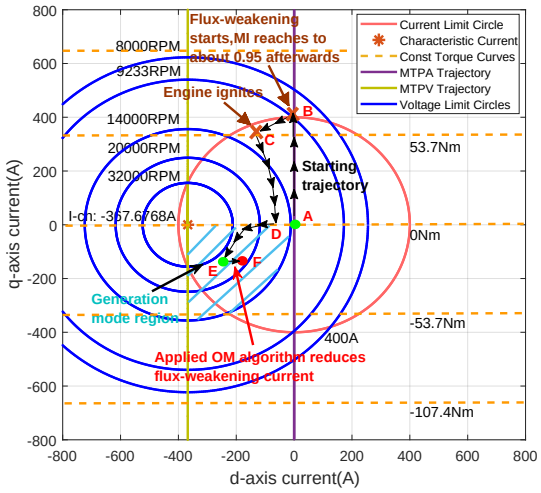

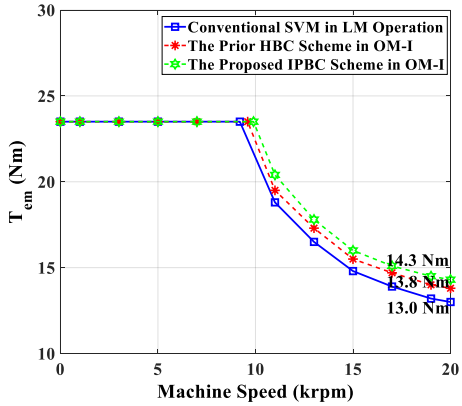

Fig. 15. (a) Operating trajectory of the ESG system. (b) Output torque capability curves of the 3L-NPC converter-fed PMSM drives.

operation of the ESG system into the overmodulation region, while the ripple in i_q is unavoidably increased, which trades an enlarged converter output voltage range against output harmonics. The experimental comparison with the same θ_c is performed at a machine speed of 20 krpm, while in order to validate the DC-link voltage utilization improvement by the IPBC scheme and the correctness of $m{=}f(\theta_c, \lambda)$ shown in Fig.10, the λ of the prior scheme and the presented one refer to 0.97 and 0.95, respectively. Besides, the test can demonstrate that a more reduced flux-weakening current is achieved with a lower compression factor for the IPBC scheme owing to a higher output modulation index. As evident in the results from Fig.14(b), both methods can lower i_d, whereas the provided algorithm, contributing to further deepen 1.5% of modulation depth, brings this value from -115A to -107.5A, as opposed to i_d of -110A with the HBC scheme at the same operating conditions. Moreover, it can be observed that the ripple of i_q by the IPBC scheme is smaller than the HBC counterpart.

B. The Operation of High-Speed Machine

The whole operating trajectory and relevant limits given by (4) and (5) are shown in Fig.15(a). In the startup process, denoted as the constant torque region, the maximum torque per amp (MTPA) line is followed by point A. The flux-weakening control activates at point B in the constant power region. Then, the trajectory tracks the voltage limits based on the PMSM

This article has been accepted for publication in a future issue of this journal, but has not been fully edited. Content may change prior to final publication. Citation information: DOI 10.1109/TPEL.2021.3105752, IEEE Transactions on Power Electronics

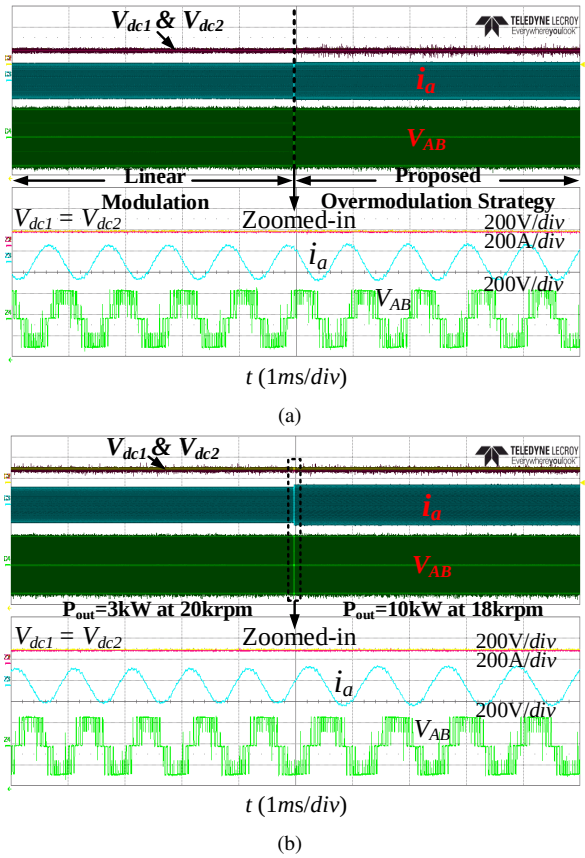

Fig. 16. (a) Steady-state performance. (b) Transient-state performance.

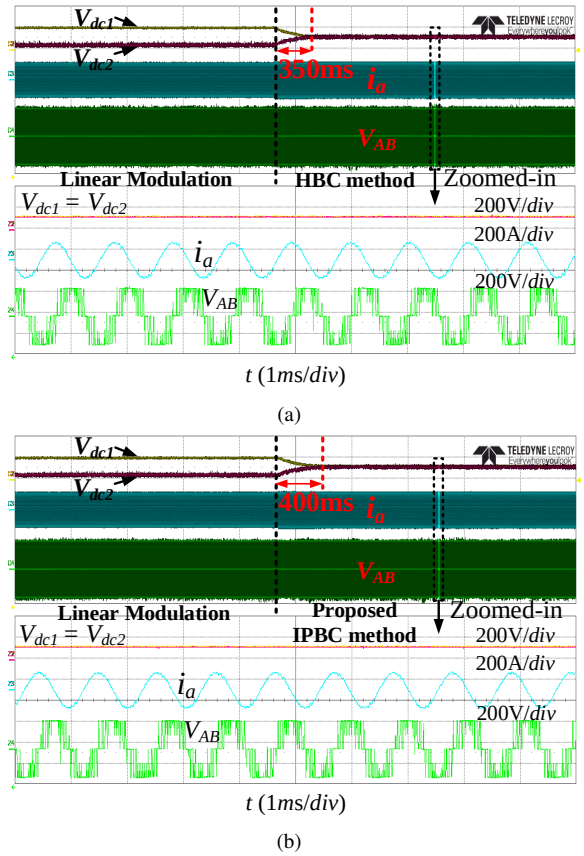

Fig. 17. NP voltage balancing process with: (a) The HBC method. (b) The proposed IPBC method.

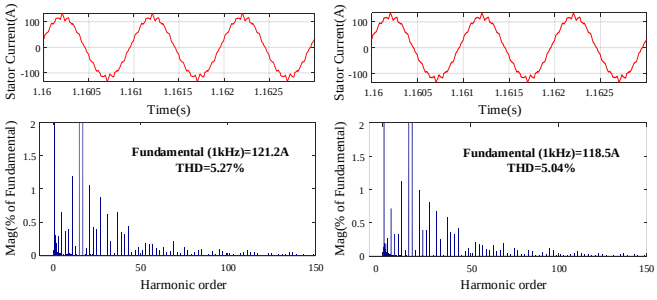

Fig. 18. FFT analysis of stator current under λ=0.95 and θ_c=12.5° with: (a) The HBC scheme. (b) The proposed IPBC scheme.

speed and current limits set by the converter. The ESG system is in standby mode after a machine speed of 10 krpm, which is denoted by point C. i_q maintains at zero and operation status is at point D until the generation mode starts. At that time, the S/G systems run in the power generating region and the modulation index is ramping up to 0.95. As the flux-weakening current is dropped by a boosted DC-link voltage utilization, the operating point subsequently moves from point E to F.

To be consistent with the experimentation presented in subsection-A, the maximum torque by the HBC (λ=0.97) and the IPBC (λ=0.95) scheme is measured at different machine speeds, which is helpful to demonstrate the output torque capability improvement. It can be seen from Fig.15(b) that the proposed strategy gains T_{em}=14.3Nm at a shaft speed of 20 krpm, which means the output torque capability is roughly increased by 3.6% as compared to the HBC limit. In comparison with the LM operation, the proposed modulation algorithm enhances 10% output torque capability for the studied drives.

C. Steady-State Performance

When the PMSM operates at a speed of 20 krpm, the steady-state performance under the LM (m=0.95) and the OM-I with the proposed IPBC method (λ=0.95 and θ_c=12.5°) are tested. The results from Fig.16(a) show that the line-to-line voltage by the proposed overmodulation technique features five levels and constant clamping instants in some periods. Apart from that, two capacitor voltages are well balanced.

D. Dynamic-State Performance

To validate the dynamic-state performance of the proposed overmodulation strategy, rotation speed and load are both changed, where λ and θ_c are set at 0.95 and 12.5°, respectively. Initially, the output active power of the ESG system is 3 kW under a machine speed of 20 krpm, in which the q-axis reference current command is -6A. After that, the PMSM speed descends to 18 krpm while the load is increased to 10 kW, where the q-axis reference current demand is -25A. The results from Fig.16(b) show a smooth transient performance regarding NP voltage, phase current and line-to-line voltage.

E. Capacitor Voltage Balancing Performance

The active capacitor voltage balancing performance is verified under a DC-link voltage utilization ratio of 1.02. That is, λ for the HBC and IPBC scheme is 0.98 and 0.95, while θ_c equals 12.5°. As shown in Fig.17, the initial NP voltage deviation is 200V in the LM region, with an average modulation index of 0.95 and power factor of 0.12. When switching to the proposed overmodulation strategy, the two capacitor voltages can be kept at a balanced state again.

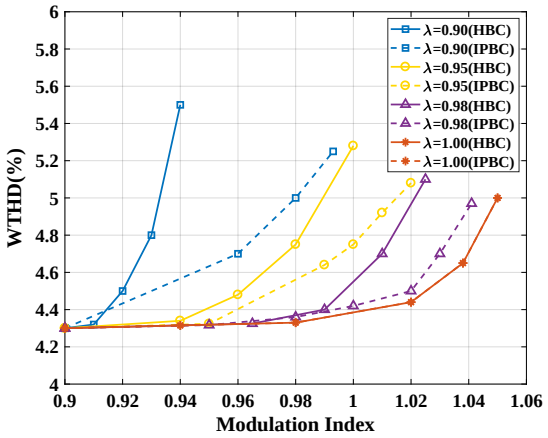

Fig. 19. WTHD comparison of line-to-line voltage at different λ and m.

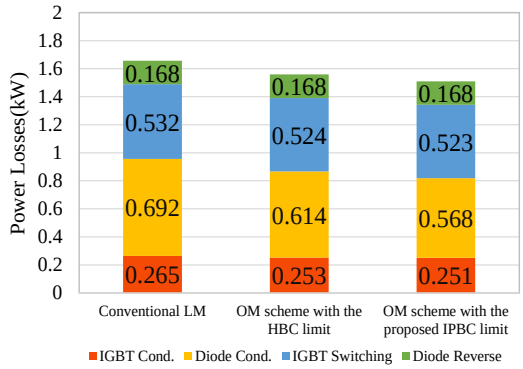

Fig. 20. The power losses comparison with different PWM schemes at 20 krpm in the generation mode.

Compared with the HBC scheme, an additional time of $50ms$ is required to correct the unbalanced NP voltage.

F. Distortion Analysis

Fig.18 presents the fast Fourier transform (FFT) analysis of the stator current when the compression coefficient is set at 0.95 and the crossover angle is controlled at 12.5°. It can be seen that the total harmonic distortion (THD) by the proposed strategy is less than that by the HBC scheme, which is consistent with the theoretical analysis in Section-III. The weighted THD (WTHD) comparison of the line-to-line voltage under different λ and desired m is illustrated in Fig.19. From the results, it can conclude that the presented inscribed polygonal-boundary limit obtains a lower WTHD as compared to the hexagonal compression limit.

G. Power Losses Analysis

Power losses analysis of the semiconductors is carried out by our applied Infineon F3L400R07ME4_B22/B23 insulated-gate bipolar transistor (IGBT) module that has the maximum collector-emitter voltage of 650V and continuous collector current of 400A. According to the manufacturer's datasheet, the losses can be obtained through the PLECS tools. Given that θ_c is set at 10°, while λ for HBC and IPBC limits is selected as 0.97 and 0.94, respectively. Switching frequency is set to be 16 kHz. Before extending into the overmodulation region, the modulation index maintains at 0.95 in the linear range. Under these operating conditions, with 35 kW of active power generation at 20 krpm, the switching device losses distribution map is elaborated in Fig.20. As can be seen, the proposed overmodulation algorithm can lower conduction losses compared with the linear range operation. Besides, due to increased DC-bus terminal clamping instants, the switching losses are reduced as compared to that by the LM. In order to experimentally test the converter's total losses under the above overmodulation conditions, a power analyzer PPA5330 is used to monitor the input and output parameters when the target system delivers an active power of 25 kW at a rotation speed of 20 krpm. A resultant of 1.24 kW power loss is measured under the presented approach, while that value in the case of the benchmark method is about 1.30 kW.

TABLE IV
ESG SYSTEM PARAMETERS

Parameters	Value
L_d = L_q	99 μH
Pole pair	3
Switching frequency	16 kHz
PM flux	0.03644 V_s/rad
Dead time	1.4 μs
Control system sampling frequency	16 kHz
Fundamental frequency in generation mode	1∼1.6 kHz
Capacitor value (C_1=C_2)	600 μF
DC-link voltage	270 V

By importing the data of stator currents into the finite element analysis model of the employed PMSM, the machine copper loss can be calculated in a steady state. Compared with typical operation in the LM, that value is significantly decreased from 189.96W to 160.18W with the upper limit of the OM-I, which means a nearly 15.7% reduction.

As the overmodulation conditions lead to a lower required flux-weakening current, the loss issue can be thus mitigated. Nevertheless, the more boosted DC-link voltage utilization, the less output harmonic performance will be for the aviation electric power system. Consequently, it comes as a trade-off between efficiency and stability to some extent.

H. Computational Time Performance

The execution time of the proposed overmodulation algorithm is tested by the applied TMS320C6713 DSP Starter Kit with a 225MHz system clock. The results present that it costs 57.2μs to implement the presented technique in the g-h reference frame, while 73.8μs is the time to implement the same algorithm in the conventional α-β reference frame, which indicates nearly 30% computational burden reduction.

I. Comparison With Other NP Control-Based Overmodulation Strategies

Compared with existing NP control-based overmodulation strategies [25]-[31] for 3L-NPC converters, the proposed strategy embraces the following advantages:

1) As the configured switching patterns generate extra NP currents to realize net-zero NP current, the proposed capacitor voltage balancing control is effective for high modulation index and low power factor operating conditions. However, the methods in [25]-[29] can hardly achieve this target.

2) Due to the adopted nearest-three VSVs, less output distortion would be expected as compared to the work of [30] that omits space vector numbers in high output voltage region.

3) The complexity caused by massive trigonometric functions is reduced by algebraic operations in the g-h plane. While

the CBPWM scheme reported in [31] gains overmodulation conditions, the appropriate ZSVs need to be calculated.

4) With the proposed IPBC technique, the output voltage converges to the upper limit of LM, which is beneficial for smooth transition among various compression coefficients, particularly for traction and servo drives, where loading conditions and speed change frequently [31]. On the other hand, due to the non-monotonous relationship between θ_c and m shown in Fig.10, the continuity of boosted DC-link voltage utilization would be affected to some extent in comparison with the HBC scheme. Nonetheless, the minimum modulation depth by the provided strategy gaining near unity might make this issue marginal. The dedicated compensation method will be explored in our future study.

V. Conclusion

In this paper, a VSV-based PWM algorithm has been presented for the 3L-NPC converter-fed high-speed aerospace drives in the MEA, which aims at the operation of aircraft ESG systems easily extending into the overmodulation region. With the provided inscribed polygonal-boundary compression technique, the major contributions of this work lie in: 1) DC-link voltage utilization is improved under a lower crossover angle and compression coefficient, which offers further benefits of flux-weakening current and machine copper loss reduction, together with an enhanced maximum output torque for the applied PMSM. 2) In order to remain a balanced NP potential under stringent operating conditions, an active capacitor voltage control method is developed to supplement the algorithm. 3) A fast-executed approach is adopted as an alternative to overcome the computational burden caused by massive trigonometric functions in the orthogonal plane, which is helpful for semiconductors with a short switching period. The conclusions are applicable to all 3L-NPC topologies in electric motor drive systems. Simulation and experimental results confirmed the good overall performance of the proposed strategy in terms of overmodulation capability, NP voltage balance, losses, phase current and ease of use.

Appendix

The duty cycle of virtual medium vector is calculated as:

1) without hexagonal-boundary compression limit:

$$d_3 = [3(1 - \frac{\sin(60^\circ - \theta)}{\sin(120^\circ - \theta)} - \frac{\sin\theta}{\sin(120^\circ - \theta)})] = 0$$

2) with hexagonal-boundary compression limit:

$$d_3 = [3(1 - \frac{\lambda\sin(60^\circ - \theta)}{\sin(120^\circ - \theta)} - \frac{\lambda\sin\theta}{\sin(120^\circ - \theta)})] = 3(1 - \lambda)$$

Acknowledgment

The authors would like to thank the reviewers and the editors for their helpful and insightful comments on an earlier manuscript of this paper. The author F. Guo would also like to thank Dr. Xiaoyu Lang for the assistance of the machine loss calculation in this study.

References

[1] P. Wheeler, S. Bozhko, "The more electric aircraft: technology and challenges," *IEEE Electrif. Mag*., vol. 2, no. 4, pp. 6-12, Dec. 2014.

[2] S. S. Yeoh, M. Rashed, M. Sanders and S. Bozhko, "Variable-voltage bus concept for aircraft electrical power system," *IEEE Trans. Ind. Electron*., vol. 66, no. 7, pp. 5634-5643, Jul. 2019.

[3] B. Sarlioglu and C. T. Morris, "More electric aircraft: review, challenges, and opportunities for commercial transport aircraft," *IEEE Trans. Transport. Electrific.*, vol. 1, no. 1, pp. 54-64, Jun. 2015.

[4] V. Raveendran, M. Andresen and M. Liserre, "Improving onboard converter reliability for more electric aircraft with lifetime-based control," *IEEE Trans. Ind. Electron*., vol. 66, no. 7, pp. 5787-5796, Jul. 2019.

[5] A. Deshpande *et al*., "Design of a high-efficiency, high specific-power three-level T-type power electronics building block for aircraft electric-propulsion drives," *IEEE J. Emerg. Sel. Topics Power Electron*., vol. 8, no. 1, pp. 407-416, Mar. 2020.

[6] Z. Huang, T. Duan, C. Tang and V. Dinavahi, "Modular assembly and real-time hardware emulation of on-the-move multidomain multimachine system on more-electric aircraft," *IEEE Trans. Ind. Electron.*, vol. 68, no. 2, pp. 1814-1824, Feb. 2021.

[7] I. Moir, and A. Seabridge, "Aircraft systems: mechanical, electrical, and avionics subsystems integration", *John Wiley & Sons*, 2008.

[8] S. Bozhko *et al*., "Development of aircraft electric starter-generator system based on active rectification technology," *IEEE Trans. Transport. Electrific.*, vol. 4, no. 4, pp. 985-996, Dec. 2018.

[9] A. Tripathi and G. Narayanan, "Analytical evaluation and reduction of torque harmonics in induction motor drives operated at low pulse numbers," *IEEE Trans. Ind. Electron*., vol. 66, no. 2, pp. 967-976, Feb. 2019.

[10] S. Mukherjee, S. K. Giri and S. Banerjee, "A flexible discontinuous modulation scheme with hybrid capacitor voltage balancing strategy for three-level NPC traction inverter," *IEEE Trans. Ind. Electron*., vol. 66, no. 5, pp. 3333-3343, May 2019.

[11] N. Beniwal, C. D. Townsend, G. G. Farivar, J. Pou, S. Ceballos and H. Dehghani Tafti, "Band-limited three-level modulation for balancing capacitor voltages in neutral-point-clamped converters," *IEEE Trans. Power Electron*., vol.35, no.9, pp.9739-9754, Sep. 2020.

[12] F. Guo, T. Yang, C. Li, S. Bozhko and P. Wheeler, "Active modulation strategy for capacitor voltage balancing of three-level neutral-point-clamped converters in high-speed drives," *IEEE Trans. Ind. Electron*., doi: 10.1109/TIE.2021.3065605.

[13] F. Donoso, A. Mora, R. Cárdenas, A. Angulo, D. Sáez and M. Rivera, "Finite-set model-predictive control strategies for a 3L-NPC inverter operating with fixed switching frequency," *IEEE Trans. Ind. Electron*., vol. 65, no. 5, pp. 3954-3965, May 2018.

[14] D. Zhou, C. Jiang, Z. Quan and Y. R. Li, "Vector shifted model predictive power control of three-level neutral-point-clamped rectifiers," *IEEE Trans. Ind. Electron*., vol. 67, no. 9, pp. 7157-7166, Sep. 2020.

[15] S. Busquets-Monge, J. Bordonau, D. Boroyevich and S. Somavilla, "The nearest three virtual space vector PWM—a modulation for the comprehensive neutral-point balancing in the three-level NPC inverter," *IEEE Power Electron. Lett*., vol. 2, no. 1, pp. 11-15, Mar. 2004.

[16] F. Guo, T. Yang, A. Diab, S. Yeoh, S. Bozhko and P. Wheeler, "An enhanced virtual space vector modulation scheme of three-level NPC converters for more-electric-aircraft applications," *IEEE Trans. Ind. Appl.*, doi: 10.1109/TIA.2021.3085798.

[17] J. Holtz, W. Lotzkat and A. M. Khambadkone, "On continuous control of PWM inverters in the overmodulation range including the six-step mode," *IEEE Trans. Power Electron*., vol. 8, no. 4, pp. 546-553, Oct. 1993.

[18] Dong-Choon Lee and G-Myoung Lee, "A novel overmodulation technique for space-vector PWM inverters," *IEEE Trans. Power Electron*., vol. 13, no. 6, pp. 1144-1151, Nov. 1998.

[19] K. Sun, Q. Wei, L. Huang and K. Matsuse, "An overmodulation method for PWM-inverter-fed IPMSM drive with single current sensor," *IEEE Trans. Ind. Electron*., vol. 57, no. 10, pp. 3395-3404, Oct. 2010.

[20] B. Wang, X. Zhang, Y. Yu, J. Zhang and D. Xu, "Maximum torque analysis and extension in six-step mode-combined field-weakening control for induction motor drives," *IEEE Trans. Ind. Electron*., vol. 66, no. 12, pp. 9129-9138, Dec. 2019.

[21] Jing Huang and K. A. Corzine, "Extended operation of flying capacitor multilevel inverters," *IEEE Trans. Power Electron*., vol. 21, no. 1, pp. 140-147, Jan. 2006.

[22] J. Mathew, P. P. Rajeevan, K. Mathew, N. A. Azeez and K. Gopakumar, "A multilevel inverter scheme with dodecagonal voltage space vectors

based on flying capacitor topology for induction motor drives," *IEEE Trans. Power Electron*., vol. 28, no. 1, pp. 516-525, Jan. 2013.
[23] K. Raj R, K. Gopakumar, A. K. Yadav, L. Umanand, M. Malinowski and W. Jarzyna, "A twelve concentric multilevel twenty-four sided polygonal voltage space vector structure for variable speed drives," *IEEE Trans. Power Electron*., vol. 34, no. 10, pp. 9906-9915, Oct. 2019.
[24] S. Pal *et al.*, "A cascaded nine-level inverter topology with T-type and H-bridge with increased DC-bus utilization," *IEEE Trans. Power Electron*., vol. 36, no. 1, pp. 285-294, Jan. 2021.
[25] S. K. Mondal, B. K. Bose, V. Oleschuk and J. O. P. Pinto, "Space vector pulse width modulation of three-level inverter extending operation into overmodulation region," *IEEE Trans. Power Electron*., vol. 18, no. 2, pp. 604-611, Mar. 2003.
[26] M. Saeedifard and A. Bakhshai, "Neuro-computing vector classification SVM schemes to integrate the overmodulation region in neutral point clamped (NPC) converters," *IEEE Trans. Power Electron*., vol. 22, no. 3, pp. 995-1004, May 2007.
[27] A. R. Beig, "Synchronized SVPWM algorithm for the overmodulation region of a low switching frequency medium-voltage three-level VSI," *IEEE Trans. Ind. Electron*., vol. 59, no. 12, pp. 4545-4554, Dec. 2012.
[28] R. Zhu, X. Wu, and Y. Tang, "Duty cycle-based three-level space-vector pulse-width modulation with overmodulation and neutral-point balancing capabilities for three-phase neutral-point clamped inverters," *IET Power Electron*., vol. 8, no. 10, pp. 1931-1940, Dec. 2015.
[29] C. Bharatiraja, S. Jeevananthan and J. L. Munda, "A timing correction algorithm-based extended SVM for three-level neutral-point-clamped MLI in over modulation zone," *IEEE J. Emerg. Sel. Topics Power Electron*., vol. 6, no. 1, pp. 233-245, Mar. 2018.
[30] A. K. Gupta and A. M. Khambadkone, "A simple space vector PWM scheme to operate a three-level NPC inverter at high modulation index including overmodulation region, with neutral point balancing," *IEEE Trans. Ind. Appl*., vol. 43, no. 3, pp. 751-760, May/Jun. 2007.
[31] S. K. Giri, S. Mukherjee, S. Kundu, S. Banerjee and C. Chakraborty, "An improved PWM scheme for three-level inverter extending operation into overmodulation region with neutral-point voltage balancing for full power-factor range," *IEEE J. Emerg. Sel. Topics Power Electron*., vol. 6, no. 3, pp. 1527-1539, Sep. 2018.
[32] S. Busquets-Monge, R. Maheshwari and S. Munk-Nielsen, "Over-modulation of *n*-level three-leg DC-AC diode-clamped converters with comprehensive capacitor voltage balance," *IEEE Trans. Ind. Electron*., vol. 60, no. 5, pp. 1872-1883, May 2013.

Feng Guo (S'19) received the B.Eng. degree from China University of Mining and Technology, Xuzhou, China, in 2014, and the M.Sc. (Hons.) degree from Northeastern University, Shenyang, China, in 2017, both in Electrical Engineering. Currently, he is working toward the Ph.D. degree with the Power Electronics, Machines and Control Group, the University of Nottingham, Nottingham, U.K.

His research interests include pulse-width-modulation strategy, multilevel inverters, diagnosis and fault tolerance control, high-speed motor drives and transportation electrification. From 2016 to 2017, he was a visiting student with the Chinese University of Hong Kong, Shenzhen, China. He was awarded as the Outstanding Graduate Student in 2017.

Tao Yang (SM'20) received his MEng Degree from Shanghai Jiao Tong University, China in 2008 and his Ph.D. degree in electrical engineering from the University of Nottingham, UK in 2013.

Since 2013, he has been a Researcher with Power Electronics, Machines and Control Group, University of Nottingham, where he became an Assistant Professor in 2016, and an Associate Professor in 2019. His research interests include high-speed electric motor drive control, power electronic conversion, electrical system design and optimization for more electric/hybrid/all-electric aircraft applications. His PhD research within EU Clean Sky on "Modelling electrical power system for more-electric aircraft applications" has resulted in him winning the inaugural "Clean Sky Best PhD Award" in 2016. Dr. Yang is an Associate Editor for the IEEE TRANSACTIONS ON TRANSPORTATION ELECTRIFICATION and Chinese Journal of Aeronautics.

Ahmed M. Diab (S'21) received the B.Sc. (Hons.) and M.Sc. degrees from Zagazig University, Zagazig, Egypt in 2011 and 2016, respectively. He is currently working toward the Ph.D. degree at the University of Nottingham Ningbo China and Institute for Aerospace technology (IAT), university of Nottingham, Nottingham, UK. From 2011 to 2016, he was a research and Teaching Assistant with the Department of Electrical Power and Machines, Zagazig University. His research interests include modeling, control, and stability in high-speed motor/generator systems for transportation electrification applications and in variable-speed wind generators.

Seang Shen Yeoh received his M.Sc degree in power electronics (Distinction) and Ph.D degree in electrical engineering from the University of Nottingham, United Kingdom, in 2011 and 2016 respectively. Since then, he has been a research fellow in the same university under the Power Electronics, Machines, and Controls Research Group. His current research interests are in the area of aircraft power systems, namely modelling and stability studies of complex power systems, and new control strategies for high-speed drive systems.

Chen Li (S'18) received B.Eng. degree from the University of Nottingham, Nottingham, U.K, in 2016, in electrical and electronics engineering. He is currently working towards the Ph.D. degree at the Power Electronics, Machines and Control Group, The University of Nottingham, Nottingham, NG7 2RD, U.K.

His research interests include high speed drives, aerospace power electronic converters, more electric aircrafts and sensorless control of AC drives.

Mr Li is the recipient of the Outstanding Paper Award for IEEE Transactions on Industrial Electronics 2020.

Serhiy Bozhko (M'97-SM'18) received his M.Sc. and Ph.D. degrees in electromechanical systems from the National Technical University of Ukraine, Kyiv City, Ukraine, in 1987 and 1994, respectively. Since 2000, he has been with the Power Electronics, Machines and Controls Research Group of the University of Nottingham, United Kingdom, where currently he is Professor of Aircraft Electric Power Systems and Director of the Institute for Aerospace Technology. He is leading several EU- and industry funded projects in the area of aircraft electric power systems, including power generation, distribution and conversion, power quality, control and stability issues, power management and optimization, as well as advanced modelling and simulations methods.

Patrick Wheeler (M'99-SM'11-F'21) received his B.Eng (Hons.) degree in 1990 from the University of Bristol, UK. He received his PhD degree in Electrical Engineering for his work on Matrix Converters from the University of Bristol, UK in 1994. In 1993 he moved to the University of Nottingham and worked as a research assistant in the Department of Electrical and Electronic Engineering. In 1996 he became a Lecturer in the Power Electronics, Machines and Control Group at the University of Nottingham, UK. Since January 2008 he has been a Full Professor in the same research group. He was Head of the Department of Electrical and Electronic Engineering at the University of Nottingham from 2015 to 2018. He is currently the Head of the Power Electronics, Machines and Control Research Group, Global Director of the University of Nottingham?s Institute of Aerosapce Technology and was the Li Dak Sum Chair Professor in Electrical and Aerospace Engineering. He is a member of the IEEE PELs AdCom and is currently IEEE PELS Vice-President for Technical Operations. He has published over 750 academic publications in leading international conferences and journals.